The Astronomical Journal, 123:1784–1800, 2002 March

DEEP WESTERBORK 1.4 GHz IMAGING OF THE BOOTES FIELD

W. H. de Vries,[1] R. Morganti,[2] H. J. A. Röttgering,[3] R. Vermeulen,[2] W. van Breugel,[1] R. Rengelink,[3] and M. J. Jarvis[3]

Received 2001 October 11; accepted 2001 November 29

ABSTRACT

We present the results from our deep (16 × 12 hr) Westerbork Synthesis Radio Telescope (WSRT) observations of the approximately 7 deg^2 Bootes Deep Field, centered at $14^h32^m05^s.75$, $34°16'47''.5$ (J2000.0). Our survey consists of 42 discrete pointings, with enough overlap to ensure a uniform sensitivity across the entire field, with a limiting sensitivity of 28 μJy (1 σ_{rms}). The catalog contains 3172 distinct sources, of which 316 are resolved by the $13'' \times 27''$ beam. The Bootes field is part of the optical/near-infrared imaging and spectroscopy survey effort conducted at various institutions. The combination of these data sets and the deep nature of the radio observations will allow unique studies of a large range of topics including the redshift evolution of the luminosity function of radio sources, the *K-z* relation, the clustering environment of radio galaxies, the radio/far-infrared correlation for distant starbursts, and the nature of obscured radio-loud active galactic nuclei.

Key words: catalogs — radio continuum: galaxies — surveys

On-line material: color figures

1. INTRODUCTION

One of the main goals of radio astronomy is to fully understand the physics of the population of extragalactic radio sources (RSs). Issues include the onset and demise of the radio activity and related starbursts, the influence of the environment on the characteristics of the RSs, and the appearance of the first RSs and their relation to the formation of galaxies, massive black holes, and the reionization of the universe.

Detailed investigations of complete samples of bright RSs with redshift information have been carried out over the last decades (e.g., 3CRR: Laing, Riley, & Longair 1983; 6CE: Eales 1985; Eales et al. 1997; Rawlings, Eales, & Lacy 2001) and led to many interesting discoveries. For example, it is now well established that the comoving number density of $z \approx 1$ powerful RSs is about 2 orders of magnitude larger than it is locally (see, e.g., Longair 1966; Dunlop & Peacock 1990). Another example is that the environment of RSs changes with redshift, with bright RSs at higher redshifts located in denser environments than locally (see, e.g., Best, Longair, & Röttgering 1998).

Through the selection of RSs that are bright and have very steep radio spectra (<-1.3), more than 150 powerful galaxies with $2 < z < 5.2$ have been found (De Breuck et al. 2000). The large star formation rates (Dey et al. 1997) and extremely clumpy optical/IR morphologies (Penterrici et al. 1999) provide strong evidence that these galaxies are massive galaxies close to the epoch of formation. Powerful radio emission is most likely caused by accretion onto massive black holes ($M_{BH} > 10^9\ M_\odot$; McLure et al. 1999; Laor 2000), indicating that such massive black holes formed alongside or possibly before the formation epoch of their host galaxies (see, e.g., Kauffmann & Haehnelt 2000). Recent VLT observations have revealed the existence of a large-scale structure of Lyα-emitting galaxies around the radio galaxy 1138−262 ($z = 2.2$), reinforcing the idea that high redshift radio galaxies can be used as tracers of protoclusters of galaxies (Pentericci et al. 2000).

At very faint flux densities (e.g., a few tens of μJy at 1.4 GHz) the radio source counts are dominated by the $z \lesssim 1$ starburst population (see, e.g., Richards et al. 1999). Long observations with the VLA + MERLIN (Richards 2000; Muxlow et al. 1999) and the Westerbork Synthesis Radio Telescope (WSRT; Garrett et al. 2000) reach such faint levels and have enabled important constraints to be placed on the redshifts and nature of distant starburst galaxies.

1.1. *Survey Rationale*

Our WSRT survey reaches a 1 σ detection threshold of 28 μJy at 1.4 GHz, within a factor of 2–3 of the deepest radio observations carried out so far (see Windhorst et al. 1999; Richards 2000). The surveyed area is, however, large enough (about 7 deg^2) to yield enough sources to not be severely affected by low number statistics for the RS populations under scrutiny. As can be seen in Figure 1, the composition of the radio population changes dramatically toward lower flux density limits. The higher flux levels are dominated by RSs with steep spectra (<-0.5), and a crossover to flat-spectrum sources appears to occur at the 10–100 mJy (at 325 MHz) level. The former are mostly identified with (powerful) radio sources residing in massive elliptical galaxies (see, e.g., Eales et al. 1997), whereas the latter can be tied to a population of star-forming late-type galaxies, especially toward sub-mJy 1.4 GHz flux density levels (see, e.g., Windhorst et al. 1999; Richards et al. 1999). Therefore, deeper observations will not only increase the number of detected sources but will also provide a better handle on the relative makeup of the radio population at μJy flux density levels.

[1] Lawrence Livermore National Laboratory/IGPP, 7000 East Avenue, L-413, Livermore, CA 94550; devries1@llnl.gov, vanbreugel1@llnl.gov.

[2] ASTRON, P.O. Box 2, 7990 AA, Dwingeloo, Netherlands; morganti@nfra.nl, rvermeulen@nfra.nl.

[3] Leiden Observatory, P.O. Box 9513, 2300 RA, Leiden, Netherlands; rottgeri@strw.leidenuniv.nl, rengelin@strw.leidenuniv.nl, jarvis@strw.leidenuniv.nl.

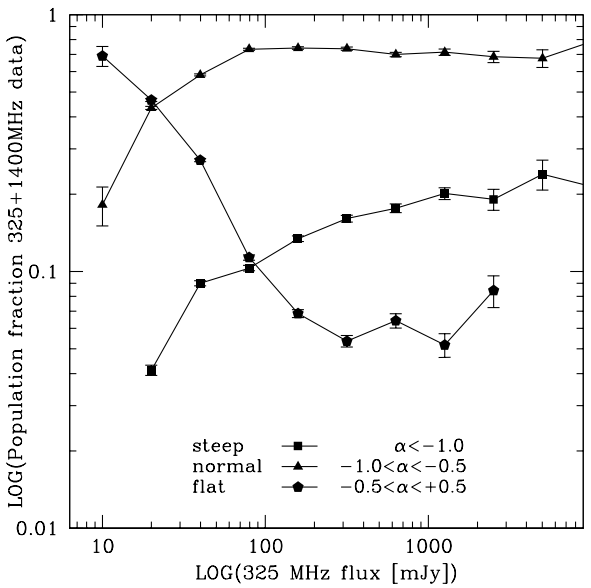

FIG. 1.—Composition of the radio source population as function of 325 MHz flux. The fraction of flat-spectrum sources increases dramatically with decreasing flux, whereas the steep-spectrum component (dominated by AGNs) drops precipitously. Data are from the source overlap between the WENSS and NVSS surveys at 325 and 1400 MHz, respectively. The error bars represent Poissonian errors and may be smaller than the symbol size in some cases. Note that WENSS sample incompleteness sets in around 20 mJy, affecting the steep source count most.

The radio source population properties do not only change as a function of flux density, they also vary with redshift. Using radio luminosity functions for active galactic nuclei (AGNs; Dunlop & Peacock 1990) and starbursting populations (Hopkins et al. 1998), we can model the expected source counts for a given redshift (and limiting flux density). This is plotted in Figure 2 for a limiting flux density of 140 μJy. Beyond a redshift of $z \sim 0.3$ the number counts for our survey are expected to be dominated by the AGN population. The combination of information presented in Figures 1 and 2 makes it clear how dependent on limiting flux density a perceived radio source population is. Indeed, for a limiting flux density of 1 mJy (at 1.4 GHz), the population is dominated by AGN-type sources at all redshifts (Hopkins et al. 1998).

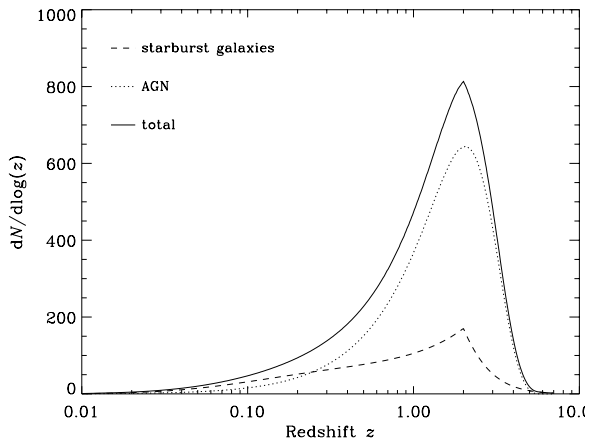

FIG. 2.—Expected redshift distribution of the radio source population for our survey, based on the luminosity functions of Dunlop & Peacock (1990; pure luminosity evolution model) and Hopkins et al. (1998; the Phoenix Survey).

The survey can detect radio sources at the FR I/FR II break level (10^{25} W Hz^{-1} at 1400 MHz; Owen & White 1991) out to a redshift[4] of $z \sim 3$. Fainter FR I–type sources with a mean radio power of 10^{24} W Hz^{-1} drop out of the sample around $z \approx 1$, and the much fainter star-forming systems will not be detected beyond $z \sim 0.15$ at the 10^{22} W Hz^{-1} level. The local starbursting system M82 has, for comparison, a radio spectral power of $10^{21.99}$ W Hz^{-1}, given its 1400 MHz flux density of 8.363 Jy (White & Becker 1992) and the adopted cosmology. Thus, the survey provides ample data for evolutionary studies of *radio-loud* systems out to at least a redshift of 1, whereas a more complete census of radio sources down to the spiral/starburst level has to be limited to sources within $z \sim 0.1$.

1.2. *Relation to Nonradio Surveys*

Key ingredients for follow-up studies are optical/near-infrared identifications and redshift information for at least a large fraction of the radio sources. For this purpose, a number of other surveys are being either carried out or planned for the same part of the sky. These include the following:

The NOAO Deep Wide-Field Survey (PIs Jannuzi and Dey).—This survey consists of a northern and a southern part, with the former field located in Bootes (near the north Galactic pole), covering a $3^\circ \times 3^\circ$ region, and the latter located in a $2^\circ \times 4.^\circ5$ equatorial region in Cetus. Both fields have been selected for their low mid- to far-infrared cirrus emission, their low H I column densities, and the availability of high-resolution ($\sim 5''$) VLA-FIRST survey radio data. Of particular interest to our program is the Bootes field, which will be imaged to a limiting surface brightness of about 28 mag arcsec^{-2} in B, V, and R and down to $\sim$22 mag arcsec^{-2} in J, H, and K. These detection limits will permit the optical and near-infrared study of faint, sub-L_* galaxies out to redshifts of about unity (an L_* galaxy will have $K = 19.82$ at $z = 1$ based on an absolute magnitude of $K = -24.44 \pm 0.06$; see Kochanek et al. 2001). The typical host galaxies of luminous radio sources, with masses well in excess of L_* galaxies, can be detected out to very large redshifts (based on the K-z diagram; see, e.g., Jarvis et al. 2001; De Breuck et al. 2002). Given our radio source population mix of powerful radio sources associated with intrinsically bright galaxies at high redshift and less luminous star-forming systems at much lower redshifts, we expect to be able to detect optical/near-infrared counterparts for most of them. The NOAO survey limits are well matched to our expected counterpart population.

The IRAC Shallow Survey (PI Eisenhardt).—The Bootes field will be covered by *SIRTF*'s Infrared Array Camera (IRAC) in four IR bands ranging from 3.6 to 8 μm. Coverage toward the longer IR bands up to 160 μm will be provided by the Multiband Imaging Photometer (MIPS), and some spectroscopy by the Infrared Spectrograph (IRS; PI in both cases is J. Houck).

The NOAO and *SIRTF* wide-field surveys are aimed to study, among other things, (1) the evolution of large-scale structure from $z \sim 1$ to 4, (2) the formation and evolution of

[4] We adopt $H_0 = 65$ km s^{-1} Mpc^{-1}, $\Omega_M = 0.3$, and $\Omega_\Lambda = 0.7$ throughout this paper.

elliptical and star-forming galaxies, and (3) the detection of very distant ($z > 4$) young galaxies and quasars. The *SIRTF* IRAC and MIPS observations will also detect star-forming galaxies at mid- to far-infrared wavelengths. It is this multi-wavelength aspect of the project, covering a large fraction of the electromagnetic spectrum (two radio frequencies, several optical and near-infrared bands, and the mid- to far-infrared space-based *SIRTF* observations) that distinguishes this effort from other deep radio-optical/near-infrared surveys like the Phoenix Survey (Hopkins et al. 1998; Georgakakis et al. 1999), and the Australia Telescope ESO Slice Project (ATESP; Prandoni et al. 2000a, 2000b, 2001).

1.3. *Relation to Other Radio Surveys*

The Bootes field has been covered by previous radio surveys, most notably by the Westerbork Northern Sky Survey (WENSS; Rengelink et al. 1997) at 325 MHz and the NRAO VLA Sky Survey (NVSS; Condon et al. 1998) and the Faint Images of The Radio Sky at 20 cm Survey (FIRST; Becker, White, & Helfand 1995), both at 1.4 GHz. A comparison between the literature surveys and our Bootes surveys (WSRT at 1.4 GHz in this paper and VLA 325 MHz) is shown in Figure 3 and tabulated in Table 1. The varying survey depths and frequencies make combining catalogs to obtain spectral index information less than straightforward. For instance, combining NVSS and 87GB (at 5 GHz; Gregory & Condon 1991) only makes sense if one is interested in radio sources with strongly inverted spectra. For our purpose, since the bulk of the radio source population has a spectral index of around -0.75 (see Fig. 10), a combination of surveys like the WENSS and NVSS/FIRST is best, as can be inferred from the overplotted common radio spectra in Figure 3.

However, these surveys do not go deep enough to effectively probe the transition in radio source population occurring around the 1 mJy level (see Figs. 1 and 9 and, e.g., Windhorst et al. 1999). Our WSRT observations do go deep enough but will need low-frequency data of matching sensitivity. We use the VLA at 325 MHz for this purpose, and the data from this program will be described in an subsequent paper. However, both the NVSS and FIRST survey data have been used to calibrate our survey flux densities and positions (see §§ 4.1 and 4.2).

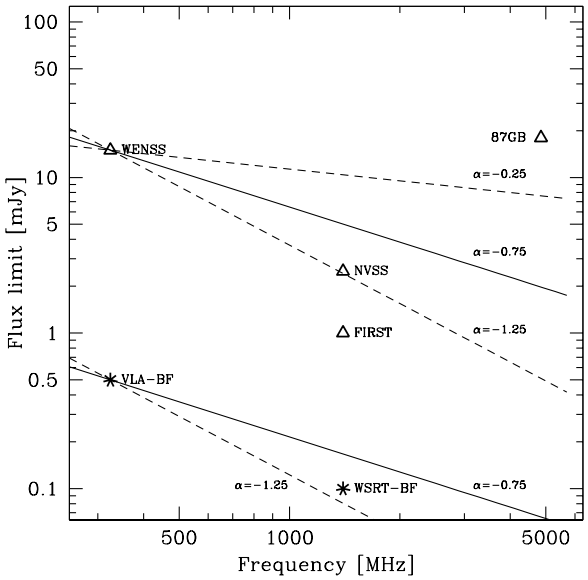

FIG. 3.—Comparison of the various radio surveys covering the Bootes field. The triangles represent literature surveys, and the stars are our Bootes WSRT and VLA surveys. Overplotted are representative radio spectra with varying spectral indices: $\alpha = -0.25$, -0.75, and -1.25 for flat-, normal-, and steep-spectrum radio sources, respectively. Any given radio source in the VLA-BF survey with a slopes shallower than -1.25 should also be present in WSRT-BF. On the other hand, of the sources in WSRT-BF fainter than the VLA-BF limit ($\sim$0.5 mJy), only the objects with slopes steeper than -1.25 should be present in VLA-BF.

2. OBSERVATIONS

The observations were carried out by the WSRT operating at 1.380 GHz. The WSRT consists of 14 25 m telescopes arranged in a 2.7 km east-west configuration. As the back end, we used the digital continuum back end with eight subbands of 10 MHz bandwidth each. The smallest baseline (9-A) was set to 54 m to limit shadowing at the expense of a reduction in large spatial structure sensitivity ($\sim$800″ for this minimum baseline and frequency).

2.1. *Field Layout and Instrumental Setup*

We designed a survey layout consisting of 42 discrete pointings. The separation between the grid points was chosen to be 60% of the FWHM of the primary beam. Given the used tiling and the known attenuation of the beam, a more or less uniform noise background is obtained

TABLE 1
COMPARISON BETWEEN VARIOUS RADIO SURVEYS COVERING THE BOOTES FIELD

Survey	Frequency	Resolution (arcsec)	Flux Density Limit[a] (mJy)	Detections in Bootes Field[b]
WENSS	325	54 × 99	15	180
VLA-Bootes	325	6	0.5	1200[c]
NVSS.....	1400	45	2.5	438
FIRST	1400	5	1.0	749
WSRT-Bootes	1400	13 × 27	0.140	3172
87GB	4850	222 × 198	18	22

[a] The 5 σ detection limit.

[b] The number of radio sources/components within a circular aperture with a radius of 5400″, centered on $14^h32^m05^s.75$, $34°16'47''.5$. Note that this number is depending on both flux limit and resolution.

[c] Expected.

with this spacing (85% of the survey area has a local rms within $\sqrt{2}\ \sigma_{\rm median}$; see § 4.3 and Fig. 8). This strategy is similar to the one used for the Australia Telescope Compact Array (ATCA) ATESP survey (see Prandoni et al. 2000a for a detailed description). The total number of pointings (42) was dictated by the need to cover the 325 MHz VLA primary beam with a uniform sensitivity (noise) level.

During each observing block of 12 hr, the telescopes were continuously cycled between three individual grid positions. This "mosaicing" mode (Kolkman 1993) allows multiple fields to be observed while still retaining a 12 hr *u-v* coverage for the fields individually (albeit sampled noncontinuously). The basic integration time for the observations is 10 s. A typical observing cycle can be broken down to a 10 s slew time between the grid positions and 5×10 s on-source time. Even though the net slewing time is less than 10 s, some extra time is needed for the array to settle itself after the move. The observing efficiency with this scheme is therefore 83.3%, resulting in 3×200 minutes net observing time per 12 hr cycle. Given the total allocated time for this project (192 hr), we used the remaining two 12 hr blocks to cycle through *all* 42 positions. In this setup, each position was revisited every 42 minutes (instead of every 3 minutes), resulting in a rather sparse *u-v* sampling and less than 15 minutes on-source time per block.

Each 12 hr block was sandwiched between two phase and polarization calibrators, typically 3C 286 and 3C 147, more than adequate given the system stability. A log of the observations can be obtained from the ftp site (see § 4).

3. REDUCTION

The mosaic was reduced, calibrated, and assembled using the MIRIAD (Sault, Teuben, & Wright 1995) software package. The data was typically of high quality, and only a few percent had to be flagged. Usually the bad data was concentrated in channel 5 (of the eight), which around 1380 MHz, is the frequency band most affected by interference due to the Global Positioning System. Every field pointing was mapped using a multifrequency synthesis approach, where the measurements of the eight bands individually are gridded simultaneously in the *u-v* plane. This significantly reduces bandwidth smearing problems. Then a three-step iterative phase self-calibration cycle was used, using typically around 100,000 clean iterations. The clean was done down to the 3 σ level so as not to incorporate too much flux in faint sources that does not belong there. In the few fields with strong sources present we performed amplitude self-calibration as well; in all other cases this did not improve the final outcome. In the fourth, and final, cycle, spectral index effects on beam shape were taken into account (Sault & Conway 1999). The final maps improved significantly by correcting for the small primary-beam shape variations across the eight 10 MHz wide frequency channels.

After all the field pointings were reduced in this manner, they were assembled into a final mosaic. This step basically adds up the maps after performing the proper primary-beam correction. Since the dirty beam changes slightly across the field, we restored all the data with a fixed synthesized beam of $13\farcs0 \times 27\farcs0$ at a position angle of 0°. The mosaic was then further mapped onto $4'' \times 4''$ pixels for a total of $\sim 2750^2$ pixels.

4. RESULTS

We used automated routines for the source extraction and catalog creation. These were slightly modified from their WENSS counterparts, but the applied methods are exactly the same, all of which are described in detail in Rengelink et al. (1997).

The software works on rectangular patches of sky only, so we tiled the circular beam into three rectangular areas, as outlined in Figure 8. All of the low-noise areas have been included this way, and only a few parts of the noisy edges have not been cataloged. The total cataloged survey area covers 6.68 deg^2.

Part of the catalog, to illustrate its format, has been listed in Table 2.[5]

4.1. *Flux Accuracy and Error Estimates*

We have compared the flux densities of unresolved sources present in both our uncalibrated Bootes and the NVSS catalog. Since the resolution of NVSS (at 45″) is slightly worse than ours ($13'' \times 27''$), a source that is unresolved in our catalog is consequently unresolved in NVSS. While we could compare our fluxes to the deeper FIRST data, the latter's much higher angular resolution typically resolves point sources in our catalog, making a direct comparison difficult. The results of the comparison are plotted in Figure 4. It is clear from the plot that our uncalibrated fluxes are a little too high in comparison to the NVSS fluxes, at least for $S > 10$ mJy. Below these fluxes, the NVSS values are systematically too high and are presumably due to a combination of Malmquist and clean biases. This overestimate of

[5] The full version (with 3172 sources) can be obtained through anonymous ftp to ftp://ftp.nfra.nl/pub/Bootes. The complete mosaic, individual pointing maps, and tables with various additional data are available from the same address, all of which are described in the README file.

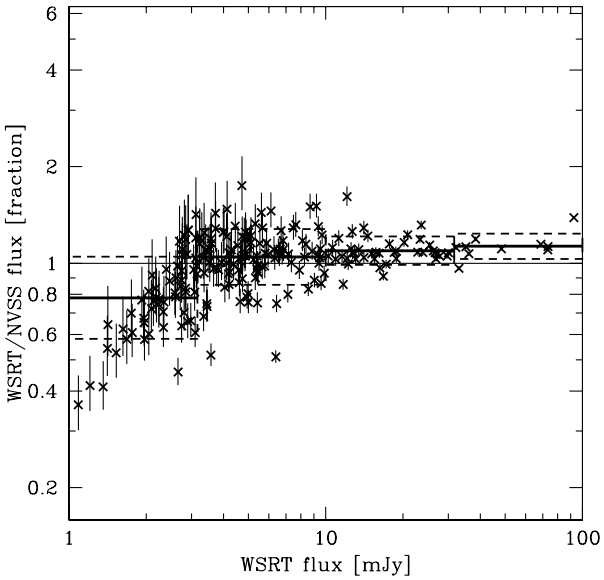

FIG. 4.—Flux density comparison between sources in common to NVSS and WSRT. Only unresolved WSRT sources (and hence unresolved in NVSS) have been included. The increase in NVSS flux density relative to the WSRT close to its detection limit is possibly due a combination of Malmquist and NVSS clean biases. Error bars are 1 σ errors and may be smaller than the symbol size in some cases.

TABLE 2

RESOLVED SOURCES WITH FLUX DENSITIES GREATER THAN 10 mJy

Source	R.A. (J2000.0)	Decl. (J2000.0)	δPOS (arcsec)	F[a]	F_{int} (mJy)	rms[b] (mJy)	Θ_{maj}[c] (arcsec)	Θ_{min}[c] (arcsec)	P.A. (deg)	LAS[d] (arcsec)
J142541+345826....	14 25 41.40	+34 58 26.6	0.4	M	262.60 ± 10.5	0.102	244	89	27	243
J142607+340424....	14 26 07.73	+34 04 24.0	0.4	M	37.73 ± 1.51	0.048	111	49	164	108
J142610+333936....	14 26 10.88	+33 39 36.6	0.4	M	29.78 ± 1.19	0.050	159	67	155	157
J142620+344012....	14 26 20.94	+34 40 12.6	0.4	M	87.01 ± 3.48	0.034	231	77	130	229
J142639+344318....	14 26 39.42	+34 43 18.6	0.4	M	15.88 ± 0.64	0.031	150	91	22	148
J142650+332941....	14 26 50.53	+33 29 41.6	0.4	M	13.41 ± 0.54	0.038	103	60	22	99.4
J142656+352230....	14 26 56.47	+35 22 30.9	0.4	M	11.31 ± 0.46	0.066	177	76	172	175
J142659+341159[e]...	14 26 59.96	+34 11 59.4	0.4	E	305.74 ± 12.2	0.042	229	81	48	227
J142702+333346....	14 27 02.23	+33 33 46.1	0.4	E	11.73 ± 0.47	0.034	243	73	46	241
J142702+345905....	14 27 02.24	+34 59 05.2	0.4	M	21.14 ± 0.85	0.031	150	56	179	148
J142716+331411....	14 27 16.20	+33 14 11.5	0.4	M	29.81 ± 1.19	0.049	145	90	140	142
J142739+330750[e]...	14 27 39.33	+33 07 50.3	0.4	M	43.62 ± 1.75	0.049	128	71	161	125
J142756+332141....	14 27 56.02	+33 21 41.3	0.4	M	18.77 ± 0.75	0.027	106	52	7	103
J142759+345500....	14 27 59.82	+34 55 00.7	0.4	M	32.37 ± 1.30	0.026	178	94	167	176
J142806+325936....	14 28 06.69	+32 59 36.7	0.4	M	29.93 ± 1.20	0.067	109	54	178	106
J142850+345408....	14 28 50.51	+34 54 08.6	0.4	M	11.18 ± 0.45	0.024	180	36	178	178
J142851+353029....	14 28 51.07	+35 30 29.5	0.4	M	22.95 ± 0.92	0.050	130	79	4	127
J142904+343252....	14 29 04.89	+34 32 52.4	0.4	M	12.98 ± 0.52	0.018	142	43	24	139
J142910+352945....	14 29 10.13	+35 29 45.1	0.4	M	24.37 ± 0.98	0.045	112	50	8	109
J142910+350320....	14 29 10.88	+35 03 20.6	0.4	M	43.10 ± 1.72	0.025	159	80	108	157
J142913+332641....	14 29 13.34	+33 26 41.3	0.4	M	36.06 ± 1.44	0.027	215	123	57	213
J142913+335619....	14 29 13.51	+33 56 19.6	0.4	M	18.51 ± 0.74	0.027	172	76	151	170
J142915+330351....	14 29 15.18	+33 03 51.4	0.4	M	10.71 ± 0.43	0.044	151	53	160	149
J142937+344117....	14 29 37.07	+34 41 17.9	0.4	M	15.33 ± 0.61	0.022	104	76	131	100
J142940+335713....	14 29 40.29	+33 57 13.0	0.4	M	15.76 ± 0.63	0.026	178	68	127	176
J142940+325755....	14 29 40.48	+32 57 55.6	0.4	M	14.04 ± 0.57	0.071	162	58	175	160
J142940+343632....	14 29 40.61	+34 36 32.0	0.4	M	17.68 ± 0.71	0.021	164	72	116	162
J142948+351748....	14 29 48.72	+35 17 48.3	0.4	M	13.18 ± 0.53	0.031	125	97	25	122
J142958+333109....	14 29 58.44	+33 31 09.6	0.4	M	21.92 ± 0.88	0.027	130	83	166	127
J143002+331720....	14 30 02.68	+33 17 20.2	0.4	M	11.07 ± 0.44	0.032	141	79	17	138
J143011+350019....	14 30 11.80	+35 00 19.4	0.4	M	15.40 ± 0.62	0.025	120	93	4	117
J143012+331442....	14 30 12.02	+33 14 42.4	0.4	E	185.15 ± 7.41	0.034	142	61	148	139
J143012+325551....	14 30 12.80	+32 55 51.6	0.4	M	15.43 ± 0.63	0.083	126	64	32	123
J143022+343727....	14 30 22.68	+34 37 27.0	0.4	M	16.44 ± 0.66	0.023	99	74	3	95.2
J143025+351914[e]...	14 30 25.43	+35 19 14.6	0.4	M	21.68 ± 0.87	0.033	172	130	42	170
J143048+333319[e]...	14 30 48.35	+33 33 19.9	0.4	M	46.61 ± 1.86	0.027	183	54	171	181
J143052+331320[e]...	14 30 52.10	+33 13 20.5	0.4	M	127.98 ± 5.12	0.034	222	80	174	220
J143054+350852....	14 30 54.99	+35 08 52.5	0.4	M	11.61 ± 0.47	0.028	104	59	10	100
J143103+334544....	14 31 03.64	+33 45 44.1	0.4	E	43.89 ± 1.76	0.026	443	81	60	442
J143114+343616....	14 31 14.08	+34 36 16.4	0.4	M	18.03 ± 0.72	0.023	109	50	175	106
J143130+342817....	14 31 30.34	+34 28 17.9	0.4	M	10.09 ± 0.40	0.024	169	41	173	167
J143134+351506[e]...	14 31 34.68	+35 15 06.7	0.4	M	98.43 ± 3.94	0.033	130	58	165	127
J143203+330743....	14 32 03.59	+33 07 43.7	0.4	M	12.57 ± 0.51	0.037	169	61	2	167
J143237+353032....	14 32 37.63	+35 30 32.3	0.4	M	28.30 ± 1.13	0.056	136	54	32	133
J143309+333609....	14 33 09.55	+33 36 09.8	0.4	M	11.86 ± 0.48	0.026	152	64	47	150
J143309+351517....	14 33 09.92	+35 15 17.8	0.4	E	34.40 ± 1.38	0.033	102	68	175	98.4
J143317+345108[e]...	14 33 17.83	+34 51 08.1	0.4	E	195.03 ± 7.80	0.035	244	56	136	243
J143340+334423....	14 33 40.88	+33 44 23.3	0.4	M	15.39 ± 0.62	0.029	128	80	17	125
J143341+341138[e]...	14 33 42.00	+34 11 38.1	0.4	E	170.40 ± 6.82	0.035	181	64	76	179
J143410+331144....	14 34 10.42	+33 11 44.2	0.4	M	144.96 ± 5.80	0.039	142	67	101	139
J143429+342812....	14 34 29.69	+34 28 12.2	0.4	E	18.58 ± 0.74	0.023	251	60	88	250
J143433+352136....	14 34 33.20	+35 21 36.3	0.4	M	39.99 ± 1.60	0.040	113	67	167	110
J143434+351009....	14 34 34.23	+35 10 09.6	0.4	M	71.27 ± 2.85	0.036	96	53	6	92.1
J143445+341220....	14 34 45.20	+34 12 20.3	0.4	M	41.91 ± 1.68	0.028	104	61	5	100
J143445+332825....	14 34 45.36	+33 28 25.8	0.4	M	36.54 ± 1.46	0.027	157	47	163	155
J143510+335445....	14 35 10.11	+33 54 45.2	0.4	M	40.66 ± 1.63	0.034	110	55	5	107
J143528+331145....	14 35 28.15	+33 11 45.5	0.4	M	48.45 ± 1.94	0.033	108	58	158	105
J143529+343423....	14 35 29.15	+34 34 23.1	0.4	M	47.94 ± 1.92	0.024	99	54	3	95.2
J143539+344400....	14 35 39.74	+34 44 00.7	0.4	M	26.71 ± 1.07	0.024	109	50	178	106
J143547+335536....	14 35 47.78	+33 55 36.7	0.4	M	53.21 ± 2.13	0.034	99	93	62	95.2
J143553+352359....	14 35 53.88	+35 23 59.8	0.4	M	22.30 ± 0.89	0.041	146	69	5	143
J143602+334353....	14 36 02.94	+33 43 53.2	0.4	M	11.15 ± 0.45	0.030	210	92	127	208
J143604+334539....	14 36 04.58	+33 45 39.5	0.4	M	13.84 ± 0.56	0.031	100	83	12	96.3
J143621+335949....	14 36 21.94	+33 59 49.5	0.4	E	127.08 ± 5.08	0.037	163	64	5	161

TABLE 2—*Continued*

Source	R.A. (J2000.0)	Decl. (J2000.0)	δPOS (arcsec)	F[a]	F_{int} (mJy)	rms[b] (mJy)	Θ_{maj}[c] (arcsec)	Θ_{min}[c] (arcsec)	P.A. (deg)	LAS[d] (arcsec)
J143623+352713....	14 36 23.49	+35 27 13.7	0.4	M	23.43 ± 0.94	0.060	114	55	179	111
J143626+334703....	14 36 26.19	+33 47 03.1	0.4	M	10.13 ± 0.41	0.030	140	112	117	137
J143703+343442....	14 37 03.20	+34 34 42.0	0.4	M	11.75 ± 0.47	0.026	240	43	1	238
J143718+344653....	14 37 18.98	+34 46 53.2	0.4	M	11.76 ± 0.47	0.030	126	85	2	123
J143739+343716....	14 37 39.43	+34 37 16.5	0.4	M	22.15 ± 0.89	0.032	176	69	179	174
J143749+345452[e]...	14 37 49.78	+34 54 52.9	0.4	M	41.87 ± 1.68	0.045	132	89	133	129
J143814+342002....	14 38 14.79	+34 20 02.0	0.4	M	11.83 ± 0.48	0.056	145	52	159	142
J143826+335023....	14 38 26.37	+33 50 23.6	0.4	M	15.66 ± 0.63	0.056	235	103	15	233
J143831+335654....	14 38 31.83	+33 56 54.5	0.4	M	11.68 ± 0.47	0.055	109	62	29	106

NOTE.—Units of right ascension are hours, minutes, and seconds, and units of declination are degrees, arcminutes, and arcseconds.

[a] Flag: S = point source, M = resolved, E = complex.

[b] Local sky rms.

[c] Apparent angular extent of 2.5 σ contour. Sources with $\Theta_{maj}/\Theta_{min} \approx 2$ and P.A. $\approx 0^\circ$ are considered barely resolved.

[d] Largest angular size. Resolved sources are deconvolved with the beam size, point source sizes are approximated by $LAS = \Theta_{beam}[0.04^2 + (6.0/SNR)^2]^{1/4}$; see Rengelink et al. 1997.

[e] Alternative names: J142659+341159 = 7C 1412+344; J142739+330750 = 7C 1425+333; J143025+351914 = NGC 5656; J143048+333319 = 7C 1428+337; J143052+331320 = 7C 1428+334; J143134+351506 = 7C 1429+354; J143317+345108 = 7C 1431+350; J143342+341138 = 7C 1431+344; J143749+345452 = 7C 1435+351.

NVSS fluxes close to their detection limit (~2.5 mJy) is also evident in the Condon et al. (1998) comparison of NVSS fluxes to deep WSRT (Katgert-Merkelijn et al. 1985) flux densities; see Figure 31 in Condon et al. (1998). Also, Prandoni et al. (2000b) noticed the same effect in comparing their ATCA radio survey fluxes to the NVSS values.

Using flux density weighting, we calculated the offset to be 4.5% ± 3.0% too high. We reduced our fluxes accordingly (see Fig. 5). Following Rengelink et al. (1997), the relative flux density errors can be written as

$$\frac{\sigma_S}{S} = \left[C_1^2 + C_2^2\left(\frac{\sigma_{rms}}{S}\right)^2\right]^{1/2}. \quad (1)$$

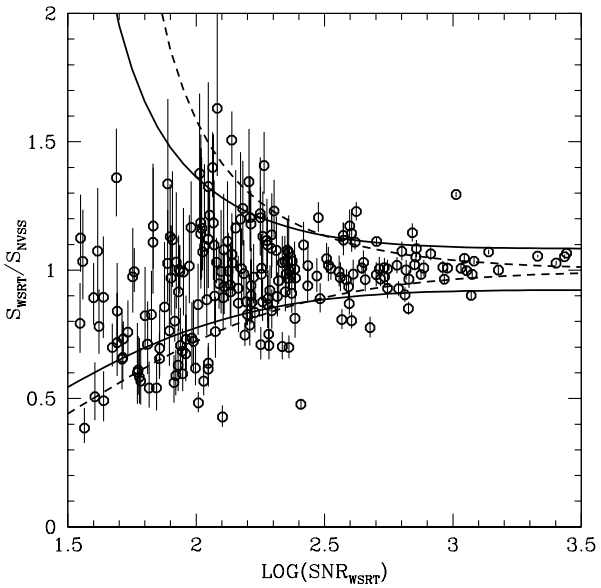

FIG. 5.—Relative flux density errors as function S/N. WSRT fluxes are compared to NVSS fluxes for unresolved radio sources present in both catalogs. The overplotted solid lines are expected upper and lower envelopes to the flux density fraction, assuming values for C_1 and C_2 (see eq. [3]) of 0.04 and 1.3, respectively. The dashed lines are for $C_1 = 0.0$ and $C_2 = 2.0$ and illustrate that C_1 is most dominant at high S/N, while C_2 is it at low S/N.

This equation reflects the two components of the measurement error, with C_1 due to a constant systematic error and C_2 being dependent on the signal-to-noise ratio (S/N). Ideally, one would like to compare our measured (and corrected) fluxes to their true values in order to determine the constants C_1 and C_2 that best fit the observed S_{WSRT}/S_{true} ratio. Unfortunately, we do not have such a control data set; instead, we use the NVSS measurements. If we assume that the NVSS measurements have a similar error dependence, we can define the flux density ratio as

$$\frac{S_{WSRT}}{S_{NVSS}} = \frac{1 \pm \left[C_1^2 + C_2^2(\sigma_{WSRT}/S_{true})^2\right]^{1/2}}{1 \pm \left[C_1^2 + C_2^2(\sigma_{NVSS}/S_{true})^2\right]^{1/2}}, \quad (2)$$

with σ_{WSRT} and σ_{NVSS} being the median noise in the sky and S_{true} the true value of the source flux. The values of σ are quoted as 0.45 mJy for the NVSS (Condon et al. 1998) and 0.028 mJy for our survey. If we further assume that S_{WSRT} and S_{NVSS} are approximately equal to S_{true} and that $(S/N)_X = S_X/\sigma_X$, with X being either WSRT or NVSS, we can rewrite equation (2) as

$$\frac{S_{WSRT}}{S_{NVSS}} = \frac{1 \pm \left\{C_1^2 + [C_2/(S/N)]^2\right\}^{1/2}}{1 \pm \left\{C_1^2 + [16.1C_2/(S/N)]^2\right\}^{1/2}} \quad (3)$$

based on $\sigma_{NVSS} = 16.1\sigma_{WSRT}$, which implies $(S/N)_{WSRT} = 16.1(S/N)_{NVSS}$. The results using equation (3) have been overplotted on Figure 5 such that the maximum (upper) envelope is given by setting the plus/minus sign to $1 + ()/1 - ()$ and the minimum envelope by $1 - ()/1 + ()$ in the equation. The C parameters have been set to 0.04 and 1.3, respectively, identical to the values in Rengelink et al. (1997). The model is most sensitive to the C_1 value, which basically sets the envelope separation at high S/N. The C_2 value, which scales the S/N dependence, is far less constrained. Values of $C_2 = 2$ (see, e.g., Kaper et al. 1966) are not excluded. Given the assumptions and the assumed uncertainties about the NVSS errors, we adopt the WENSS

values of 0.04 and 1.3. The quoted flux density errors in the final catalog are calculated with these particular values.

4.2. *Positional Accuracy*

Optical identifications can only be securely made if the radio positions are known accurately. The optical source density becomes high enough toward fainter magnitudes to effectively have one potential counterpart per beam. For instance, the mean source separation in the Deeprange *I*-band field survey is about 17″ at the 23 mag level (Postman et al. 1998). This separation is actually smaller than the WSRT beam size at 1400 MHz. Good positional matches are therefore essential.

We compared the cataloged positions for point sources against their FIRST positions and against Automatic Plate Measuring (APM) machine identifications. The APM facility (in Cambridge, UK) catalogs identifications and positions based on scanned UK and POSS II Schmidt plates, covering currently more than 15,000 deg^2 of sky.

The relative offsets for the individual sources are plotted in Figure 6. It is clear that the FIRST and APM positions agree rather well with each other (indicated by the crosses) but that our positions are systematically off in right ascension. Without more frequent observations of additional calibrators, which would adversely affect our *u-v* coverage, astrometric accuracy of the WSRT is known not to be better than about 0.″5 (see, e.g., Oort & Windhorst 1985), consistent with our offset value. We corrected all the positions in right ascension with −0.″56, i.e., the mean of the FIRST and APM right ascension offsets. This correction corresponds to about 4% of the beam width, small but significant enough when accurate positional coincidences are needed.

Analogously to equation (1) for the flux density errors, we can describe the flux density dependence on positional accuracy in the form

$$\sigma_{\alpha,\delta} = \left[C_1^2 + C_2^2\left(\frac{\sigma_{\rm rms}}{S}\right)^2\right]^{1/2} = \left[C_1^2 + C_2^2(\mathrm{S/N})^{-2}\right]^{1/2}. \quad (4)$$

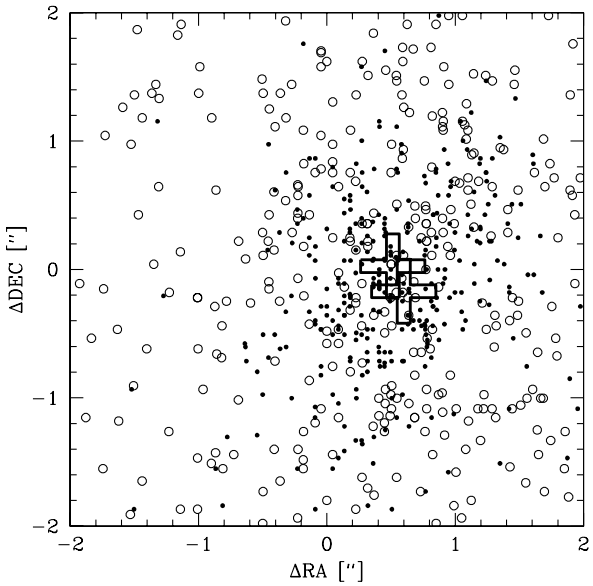

FIG. 6.—WSRT positional check against FIRST and optical APM positions. Only WSRT point sources are used. FIRST positions are indicated by the solid circles, and APM identifications are plotted as open circles. The larger scatter in the APM correlation is due to the association of radio positions with unrelated nearby optical objects. The mean offsets (indicated by the crosses) are ΔR.A. = 0.″60, ΔDecl. = −0.″17 for FIRST and ΔR.A. = 0.″51, ΔDecl. = +0.″02 for the APM match.

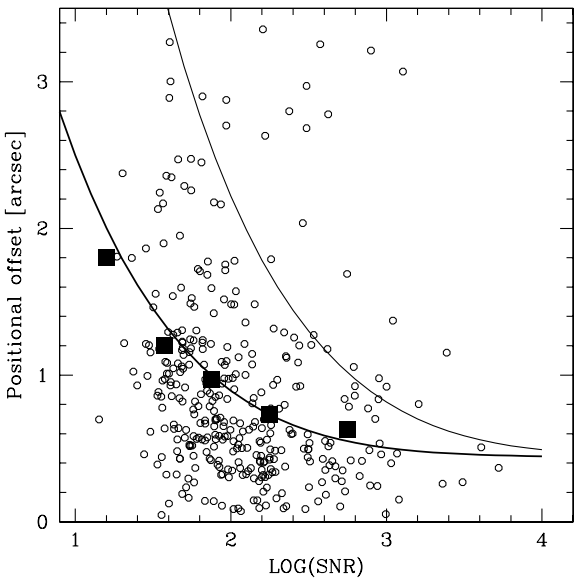

FIG. 7.—Positional offsets from FIRST/APM positions as a function of the S/N. Overplotted as solid squares are the 67% values for a given S/N. The bottom curve represents the best-fitting 1 σ error envelope (see eq. [4]), with $C_1 = 0.44$ and $C_2 = 5.5$. The top curve is identical to the one modeled for the WENSS survey (Rengelink et al. 1997).

The absolute distances from the FIRST positions have been plotted in Figure 7 as a function of S/N. Our survey positions have been corrected for the right ascension offset first. Since the FIRST resolution is higher than our survey and may lead to two (or more) FIRST catalog positions for any of our positions, we only considered FIRST point sources within our survey field. The inclusion of resolved sources (in either FIRST or our survey) unnecessarily complicates the comparison.

In Figure 7 a clear decrease in positional offset with increasing S/N can be seen. To characterize this trend, we fitted equation (4) to the 67th percentile points (*filled squares*) in order to get a 1 σ positional error estimate. The best-fitting values for the constants are $C_1 = 0.''44$ and $C_2 = 5.''5$. An outer envelope to the offset distribution is given by $C_1 = 0.''44$ and $C_2 = 15.''0$. The value for C_2 is actually the mean beam size (taken to be 20″) divided by 1.3, a value identical to the one quoted for the WENSS survey (Rengelink et al. 1997). We adopt the first set of constants (the 1 σ equivalents) for our source catalog.

4.3. *Completeness and Reliability*

The background noise in our survey is not uniformly flat but has a marked upturn toward the edges. The tiling was set up in such a way that in the interior regions the noise should be flat. This can be verified in Figure 8, which plots the actual background noise. The median noise level of the inner parts is 28 μJy. The large 30–40 μJy "intrusion" at $14^{\rm h}36^{\rm m}$, 34°00′ is most likely due to the somewhat higher noise levels in those four particular pointings.

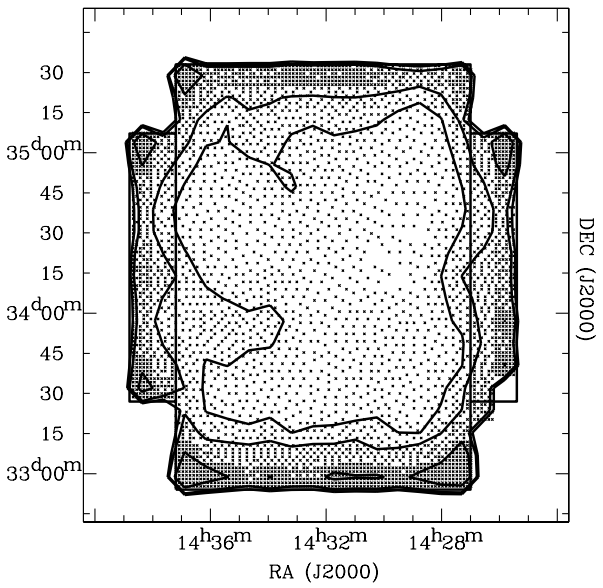

FIG. 8.—Map of the rms noise inside the source extraction area (outlined by the boxes). The noise levels and relative surface area are, from inside out, 20–30 μJy (60.9%), 30–40 μJy (23.9%), 40–80 μJy (13.3%), and 80–160 μJy (2.0%).

The survey completeness can be gleaned from Figure 9, in which the differential source counts are plotted against flux. The number counts have been normalized by the expected number in a Euclidean universe, given by $N_{\rm Eucl} = K_\nu S_\nu^{-5/2}$, with the unitless constant $K_\nu = 225$ (consistent with, e.g., Oort & Windhorst 1985 and Oort 1987, but see Wall 1994, who lists $K_\nu = 200$). Our source counts are compared to the ones based on the NVSS and FIRST catalogs, which because of their much larger survey area, extend farther toward higher flux densities. There is good agreement (within the 1 σ error bars) over the range 10–100 mJy between the surveys. The small deviation in our differential counts around the 4 mJy bin appears to be real and might indicate the presence of an overdense region within our field (e.g., a cluster). Since our survey field is relatively small at 6.68 deg^2, any local overdensity could skew the number counts significantly. The NVSS and FIRST number counts are not affected by this and serve as a useful baseline.

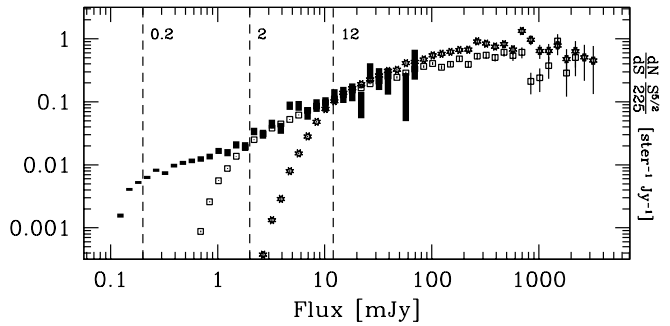

FIG. 9.—Differential source counts as function of flux density S (*vertical bars*). The counts have been normalized to the expected number for a Euclidean universe. The lengths of the vertical bars are set by the $\sqrt{N}$ error bars. Overplotted are the differential source counts for the NVSS (*stars*) and FIRST (*open squares*) surveys. Note the onset of incompleteness in NVSS at 12 mJy, in FIRST around 2 mJy, and in our survey at about 0.2 mJy.

All three plotted surveys have different completeness limits, and if one marks the first systematic deviation from a low-order polynomial fit as the completeness limit, we measure 12 mJy for NVSS, 2 mJy for FIRST, and 0.2 mJy for our survey. However, since the noise in our survey is not constant across the source extraction area but varies within the 30% level over ~90% of the survey, the 0.2 mJy value is not strictly correct. It represents a mean value over the survey area, with completeness levels slightly lower and higher in the inner and more outer parts of the survey, respectively.

4.4. *Source Confusion*

With the $13'' \times 27''$ beam size and the faint flux density levels reached in this survey, considerable source confusion might be present. We therefore modeled this by randomly distributing the cataloged source population over the survey area a large number of times (10^4–10^5). Each time the likelihood of having close pairings of sources was recorded. Given a large enough sampling, a more or less accurate estimate of the frequency of occurrence is possible. The results are given in Table 3. Since we used the actual catalog, a strong flux dependency is to be expected. In other words, having two bright ($\gtrsim$10 mJy) objects very close together almost always means that they are physically associated, whereas two faint ($\lesssim$0.5 mJy) objects with a similar separation are most likely unconnected. Based on the numbers from Table 3, we can state that sources with a double morphology, flux densities greater than 3 mJy, and angular separations of less than $1'$ have a 96% chance of being true physical doubles. All of the listed resolved sources with flux densities greater than 10 mJy in Table 2 should therefore be considered single physical entities and, hence, accurately classified.

Assuming the approximately twofold increase in unrelated object count continues toward fainter flux levels, a similar WSRT survey would become confusion-dominated (i.e., with on average two faint objects in the synthesized beam) around the 15 μJy mark. For this survey, with a 5 σ limit of 140 μJy, on average 10% of the beams are confused.

4.5. *Source Catalog*

The final catalog, which lists every source with a flux density over 5 times the local σ (corresponding to 140 μJy in the center of the survey field), contains 3172 sources. Roughly 10% of these are resolved (316) by the $13'' \times 27''$ beam. A complete breakdown of source morphology is given in Table 4. More complete catalogs with varying threshold values of σ are available from the ftp site. The total number of included sources decreases with increasing S/N limits: 3172, 2767, 2367, 2061, 1854, and 1692 sources for 5, 6,..., 10 σ thresholds, respectively. Also, detailed radio maps of the complete survey area are provided, with the cataloged sources clearly indicated. This will allow for a direct visual assessment whether a particular source is to be considered real or not.

Our survey catalog contains 143 sources that are also detected in the WENSS survey. Figure 10 plots the 325–1400 MHz spectral index distribution of these sources. The 73 brightest resolved objects have been listed in Table 2, all of which have flux densities in excess of 10 mJy. Contour plots for these particular sources are presented here in Figure 11. There appears to be a trend for

TABLE 3
SOURCE CONFUSION LIMITS.

LOWER FLUX LIMIT (mJy)	EXPECTED NUMBER OF OBJECTS WITHIN RADIUS R		
	$R = 30''$	$R = 60''$	$R = 120''$
0.05	0.11	0.43	1.70
0.10	0.10	0.43	1.69
0.20	0.074	0.29	1.18
0.40	0.041	0.17	0.65
0.80	0.025	0.097	0.38
1.60	0.012	0.057	0.23
3.20	0.0083	0.036	0.14
6.40	0.0052	0.019	0.073
12.80	0.0026	0.0090	0.039
25.60	0.0012	0.0055	0.021
51.20	0.0007	0.0024	0.0095
102.40	0.0002	0.0005	0.0031
204.80	0.00002	0.0001	0.0007

NOTE.—The listed counts are the number of unrelated objects within a search radius R around a preselected target. For the total source count within a radius R, one should therefore be added to this count. The lower two flux density bins are affected by the incompleteness of the catalog at those levels; otherwise a factor of $\sim$2 decrease in expected counts with increasing flux density threshold seems to be present. Also note the surface area factor of 4 in count levels between the columns. Objects within the $30''$ radius are too close to be resolved by the WSRT beam and would mistakenly be classified as a single source. To keep the number of significant digits approximately constant, we had to increase the number of simulations with increasing flux density threshold.

the more luminous sources (>100 mJy) to have slightly steeper spectral indices than the fainter part of the sample (<100 mJy). The actual mean values are -0.60 ± 0.31 and -0.81 ± 0.13 for the flux bins 10–100 and 100–1000 mJy, respectively. The quoted errors are the 1 σ standard deviations. This overall flattening of the spectral index with decreasing flux density levels is consistent with the data presented in Figure 1, which shows the change in radio source population as a function of flux density based on the WENSS and NVSS surveys. Unfortunately, we cannot use our much deeper survey (compared to NVSS) to extend this toward even lower flux densities. To the left of the slanted line in Figure 10 the WENSS survey was not deep enough to detect the radio sources at 325 MHz. We will use our deep VLA observations of the Bootes field for this purpose.

Ten of the radio sources in our catalog have redshifts given in the literature, and these are listed in Table 5. Alternative (radio catalog) names for some of our objects are given in the footnotes to Table 2.

TABLE 4
CATALOG MORPHOLOGY BREAKDOWN

Morphology	Number	Density Deg^{-2}	Example Object
Unresolved	2856	427.5	
Barely resolved	43	6.4	J142851+353029
Double	136	20.4	J143703+343442
Triple	13	1.9	J143309+333609
Asymmetric	112	16.7	J143604+334539
Complex/other	12	1.8	J143429+342812
Total	3172	474.9	

5. SUMMARY

We presented the results from our deep WSRT observations of the Bootes Deep Field. The survey reached a 1 σ limiting flux density of 28 μJy in the central region, and 3172 sources were detected above the 5 σ level in a 6.68 deg^2 area.

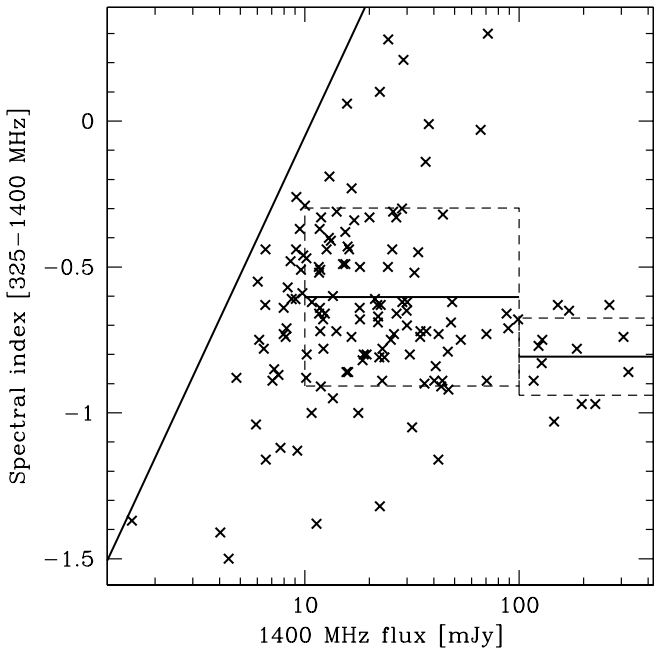

FIG. 10.—Spectral index distribution as a function of 1400 MHz flux. The 325 MHz data is from the WENSS survey. The slanted line represents the WENSS sensitivity limited spectral index using a 3 σ detection threshold of 11 mJy at 325 MHz. The two solid horizontal lines are the spectral index means for the flux density ranges 10–100 and 100–1000 mJy, respectively. The dashed boxes outline the 1 σ area.

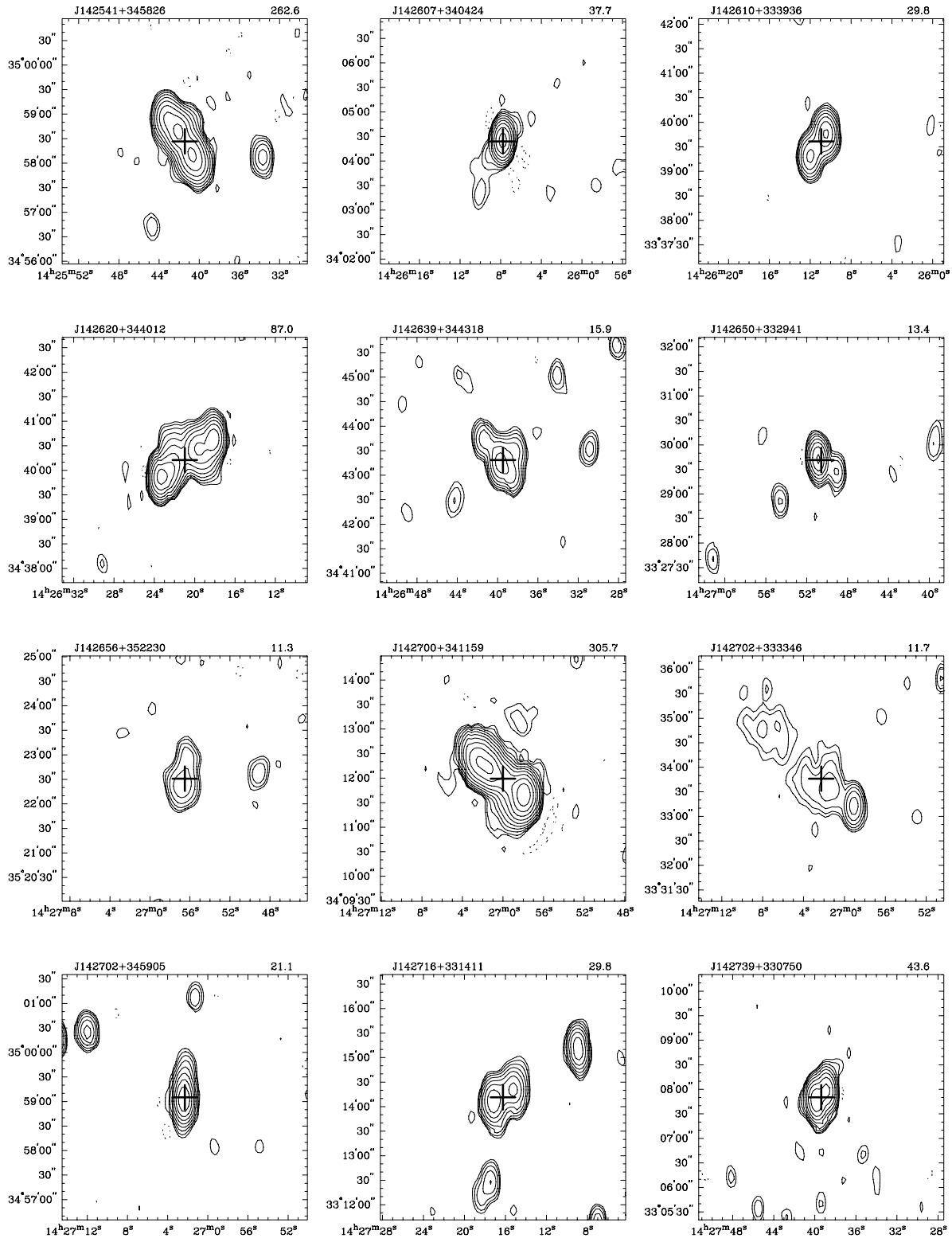

FIG. 11.—Plots of resolved sources with $S > 10$ mJy. The contour levels are given by $(1 + 2^n)\sigma$, with $n = 1, 2, \ldots$ and σ as the local background noise. Negative contours have the same spacing and are plotted as dotted lines. The cross represents the nominal source center, and the object name and 1400 MHz flux densities are given in the upper left-hand and right-hand corners, respectively.

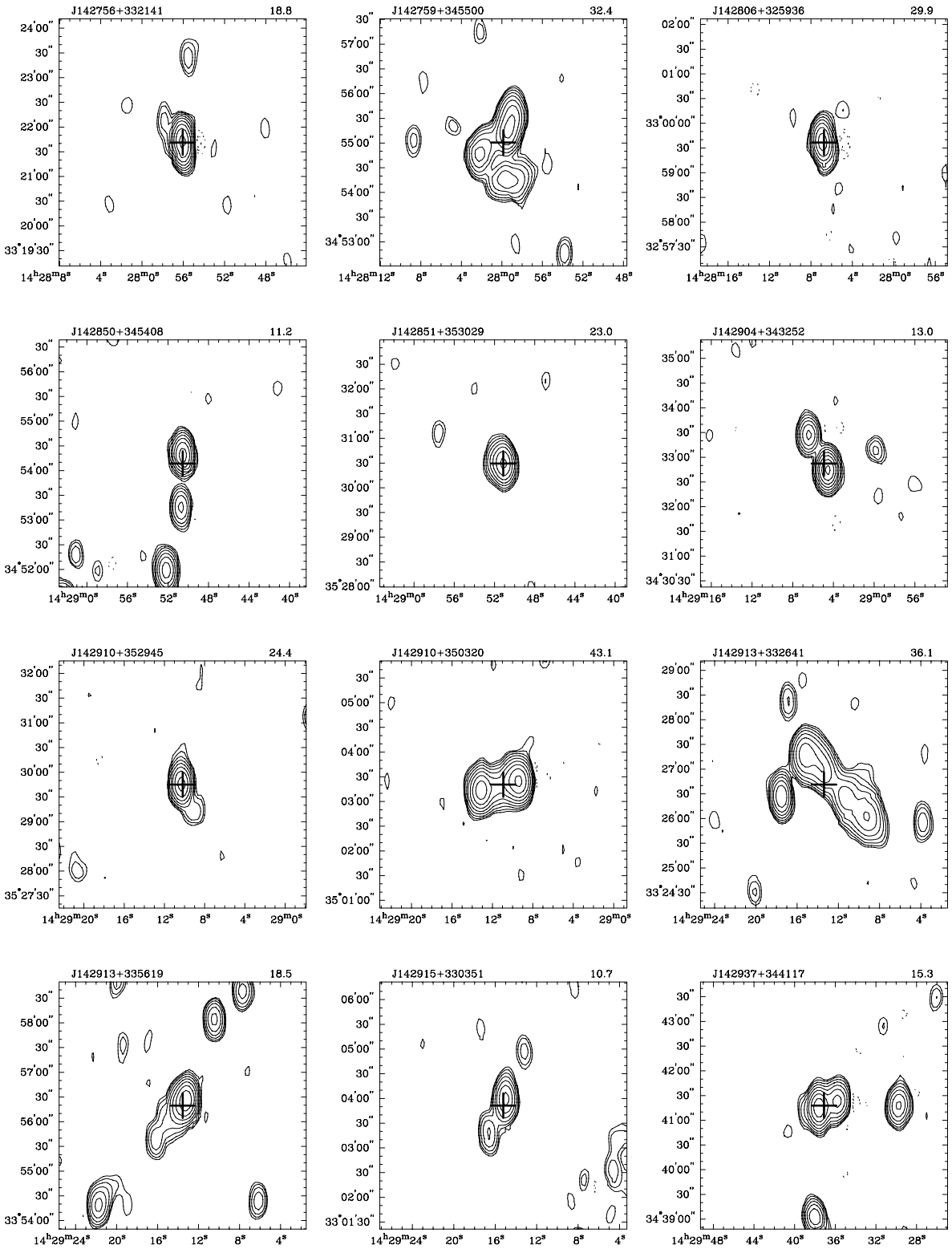

FIG. 11.—*Continued*

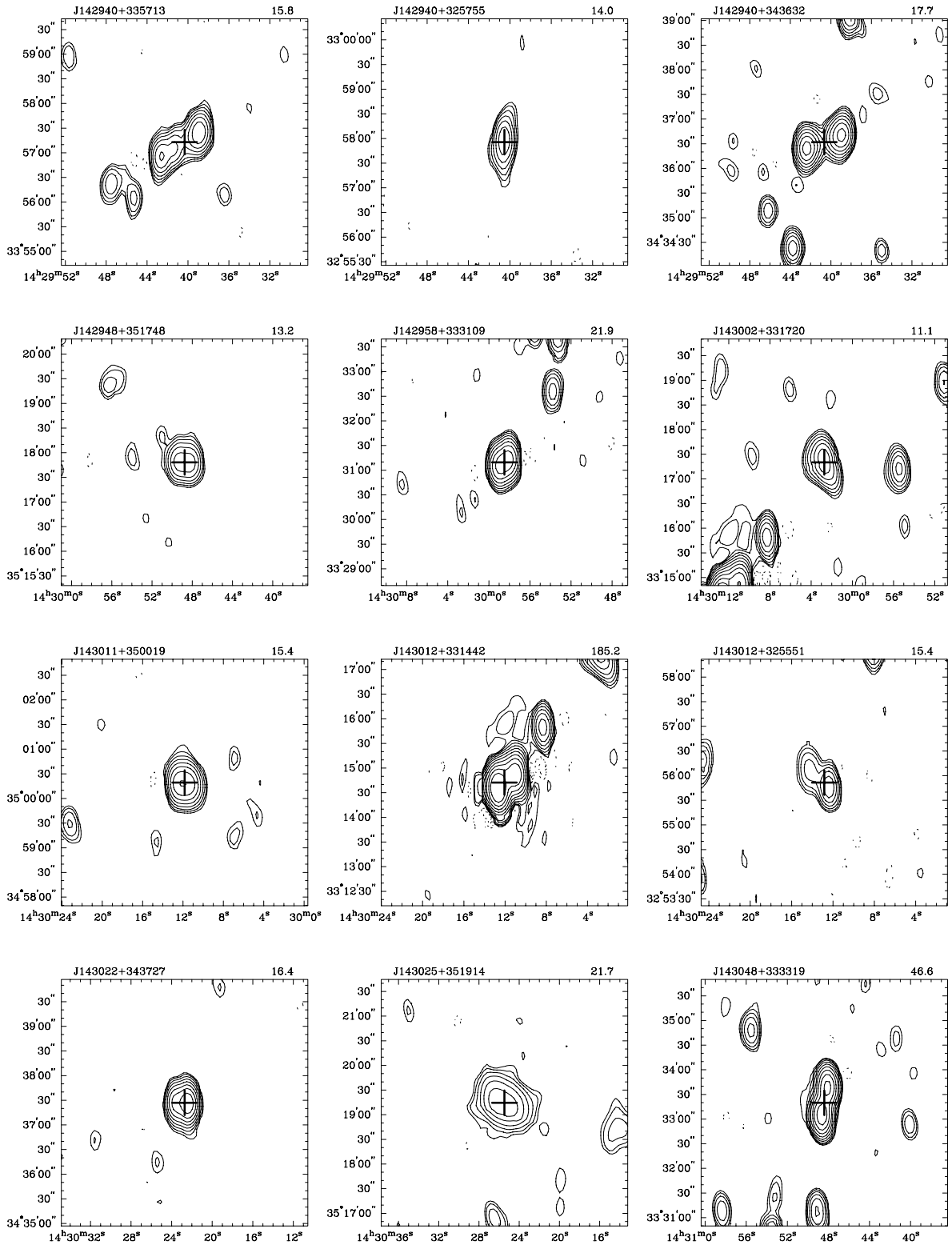

FIG. 11.—*Continued*

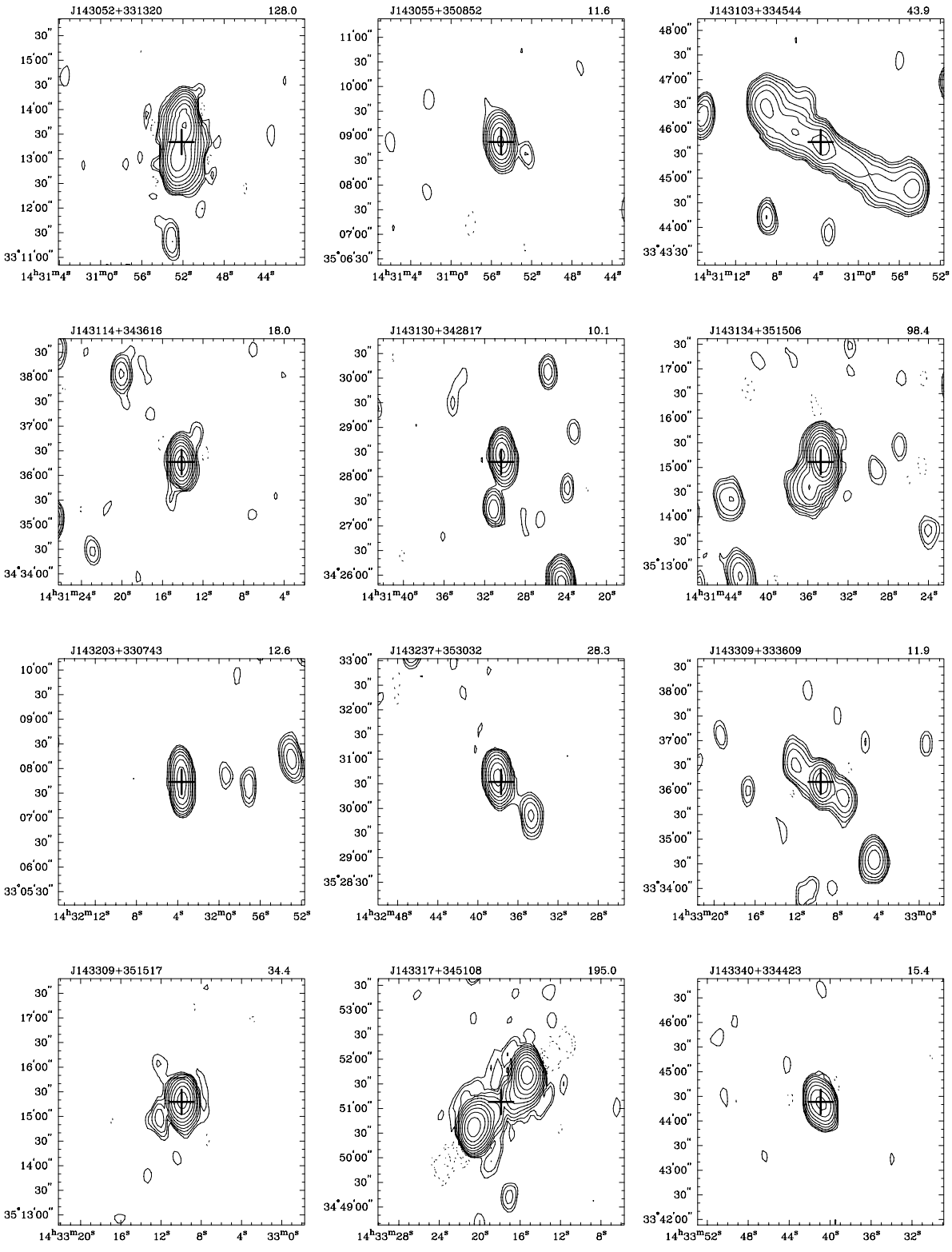

FIG. 11.—*Continued*

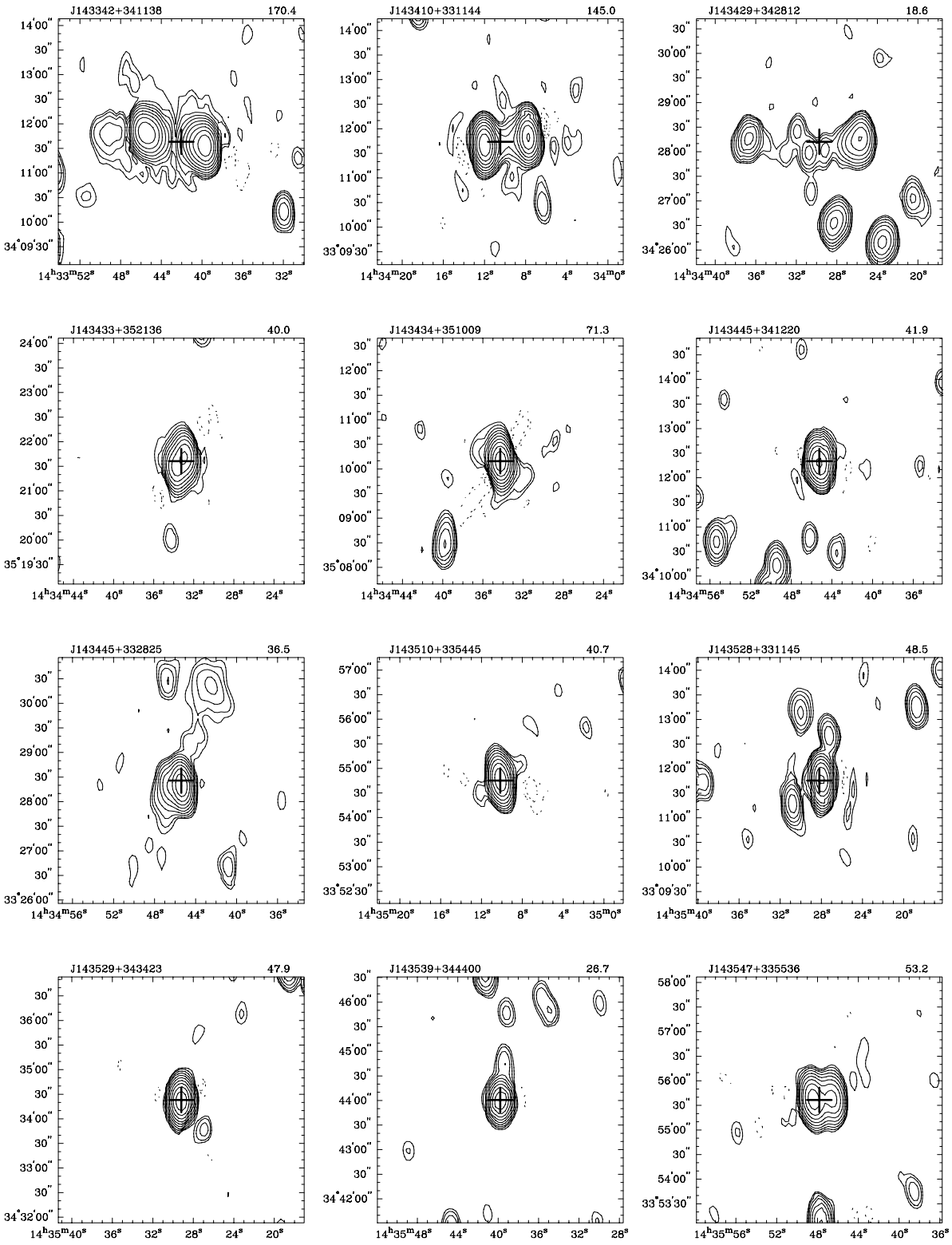

FIG. 11.—*Continued*

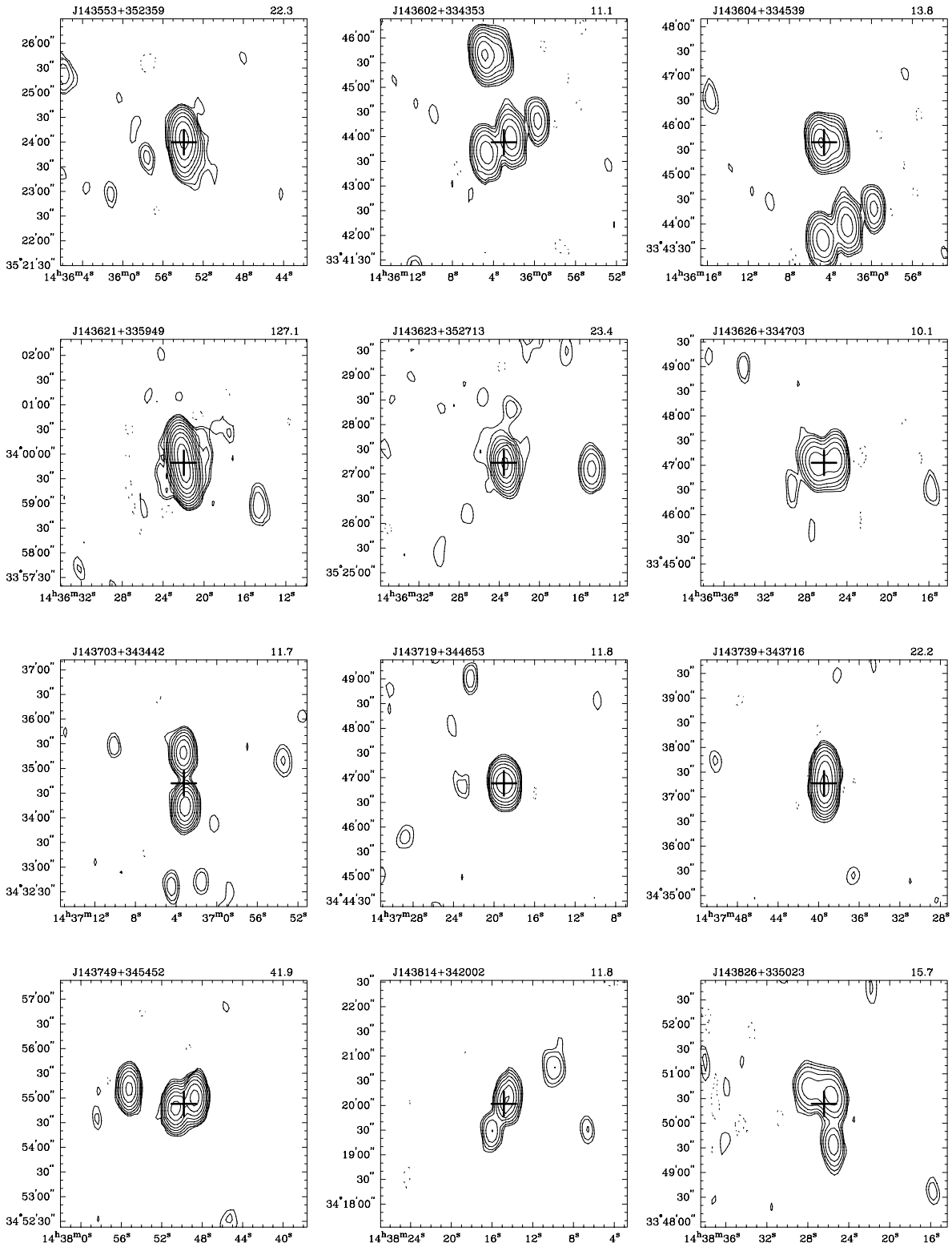

FIG. 11.—*Continued*

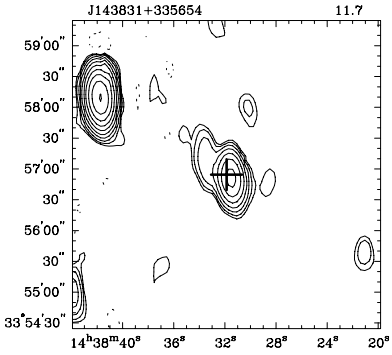

FIG. 11.—*Continued*

TABLE 5
SOURCES WITH KNOWN REDSHIFTS

Name	Alternate Name	R.A. (J2000.0)[a]	Decl.[a] (J2000.0)	ID	z	V	F_{1400}[b] (mJy)
J142744+333829.....		14 27 44.49	+33 38 29.2	G	1.237	...	14.18
J142823+331514.....	UGC 09284	14 28 23.42	+33 15 14.2	G: Sa?	0.01386	14.86	0.93
J142932+333038.....	CG 0447	14 29 32.66	+33 30 38.4	G	0.02638	17	0.12
J142934+352742.....	NGC 5646	14 29 34.07	+35 27 42.2	G: SBb	0.02861	14.99	1.37
J143025+351914.....	NGC 5656	14 30 25.43	+35 19 14.6	G: SAab	0.01051	12.73	15.33
J143119+343803.....	CG 0457	14 31 19.91	+34 38 03.9	G	0.01440	17.20	1.25
J143125+331349.....	CG 0459+0460	14 31 25.36	+33 13 49.9	G: S	0.02247	14.6	4.73
J143156+333830.....	VV 775	14 31 56.15	+33 38 30.1	G: Irr	0.03373	16	5.88
J143232+340626.....	LEDA 099838	14 32 32.42	+34 06 26.3	G	0.04264	17.96	0.21
J143518+350709.....	CG 0479	14 35 18.28	+35 07 09.2	G	0.02847	14.5	26.88

NOTE.—Units of right ascension are hours, minutes, and seconds, and units of declination are degrees, arcminutes, and arcseconds.

[a] Radio position.

[b] Radio flux, with $\sigma = 0.028$ mJy.

The survey is deep enough to sample the change in radio source population properties at the few mJy level. In combination with our lower frequency VLA data, these data sets will provide key information pertaining to, among other things, the nature and evolution of radio sources, in both the local and the high-redshift universe.

The work of W. H. D. V. and W. V. B. was performed under the auspices of the US Department of Energy, National Nuclear Security Administration by the University of California, Lawrence Livermore National Laboratory under contract W-7405-Eng-48. W. H. D. V. thanks the Nederlandse Organisatie voor Wetenschappelijk Onderzoek (NWO) for their generous allocation of his visitors grant to Dwingeloo, which got this project underway. The Westerbork Synthesis Radio Telescope is operated by the ASTRON (Netherlands Foundation for Research in Astronomy) with support from the Netherlands Foundation for Scientific Research (NWO). This research has made use of the NASA/IPAC extragalactic database (NED), which is operated by the Jet Propulsion Laboratory, Caltech, under contract with the National Aeronautics and Space Administration.

REFERENCES

Becker, R. H., White, R. L., & Helfand, D. J. 1995, ApJ, 450, 559
Best, P., Longair, M. S., & Röttgering, H. J. A. 1998, MNRAS, 295, 549
Condon, J. J., Cotton, W. D., Greisen, E. W., Yin, Q. F., Perley, R. A., Taylor, G. B., & Broderick, J. J. 1998, AJ, 115, 1693
De Breuck, C., van Breugel, W., Röttgering, H. J. A., & Miley, G. 2000, A&AS, 143, 303
De Breuck, C., van Breugel, W., Stanford, A., Röttgering, H., Miley, G., & Stern, D. 2002, AJ, in press (astro-ph/0109540)
Dey, A., van Breugel, W., Vacca, W. D., & Antonucci, R. 1997, ApJ, 490, 698
Dunlop, J., & Peacock, J. 1990, MNRAS, 247, 19
Eales, S. A. 1985, MNRAS, 217, 149
Eales, S., Rawlings, S., Law-Green, D., Gotter, G., & Lacy, M. 1997, MNRAS, 291, 593
Garrett, M. A., de Bruyn, A. G., Giroletti, M., Baan, W. A., & Schilizzi, R. T. 2000, A&A, 361, L41
Georgakakis, A., Mobasher, B., Cram, L., Hopkins, A., Lidman, C., & Rowan-Robinson, M. 1999, MNRAS, 306, 708
Gregory, P. C., & Condon, J. J. 1991, ApJS, 75, 1011
Hopkins, A. M., Mobasher, B., Cram, L., & Rowan-Robinson, M. 1998, MNRAS, 296, 839
Jarvis, M. J., Rawlings, S., Eales, S., Blundell, K. M., Bunker, A. J., Croft, S., McLure, R. J., & Willott, C. J. 2001, MNRAS, 326, 1563
Kaper, H. G., Smiths, D. W., Schwartz, U., Takakubo, K., & van Woerden, H. 1966, Bull. Astron. Inst. Netherlands, 18, 465
Katgert-Merkelijn, J., Robertson, J. G., Windhorst, R. A., & Katgert, P. 1985, A&AS, 61, 517
Kauffmann, G., & Haehnelt, M. 2000, MNRAS, 311, 576

Kochanek, C. S., et al. 2001, ApJ, 560, 566
Kolkman, O. M. 1993, The Westerbork Synthesis Radio Telescope User Documentation (Dwingeloo: NFRA)
Laing, R. A., Riley, J. M., & Longair, M. S. 1983, MNRAS, 204, 151
Laor, A. 2000, ApJ, 543, L111
Longair, M. S. 1966, MNRAS, 133, 421
McLure, R. J., Kukula, M. J., Dunlop, J. S., Baum, S. A., O'Dea, C. P., & Hughes, D. H. 1999, MNRAS, 308, 377
Muxlow, T. W. B., Wilkinson, P. N., Richards, A. M. S., Kellermann, K. I., Richards, E. A., & Garrett, M. A. 1999, NewA Rev., 43, 623
Oort, M. J. A. 1987, A&AS, 71, 221
Oort, M. J. A., & Windhorst, R. A. 1985, A&A, 145, 405
Owen, F. N., & White, R. A. 1991, MNRAS, 249, 164
Pentericci, L., et al. 2000, A&A, 361, L25
Pentericci, L., Röttgering, H. J. A., Miley, G. K., McCarthy, P., Spinrad, H., van Breugel, W. J. M., & Macchetto, F. 1999, A&A, 341, 329
Postman, M., Lauer, T. R., Szapudi, I., & Oegerle, W. 1998, in ASP Conf. Ser. 146, The Young Universe: Galaxy Formation and Evolution at Intermediate and High Redshift, ed. S. D'Odorico, A. Fontana, & E. Giallongo (San Francisco: ASP), 413
Prandoni, I., Gregorini, L., Parma, P., de Ruiter, H. R., Vettolani, G., Wieringa, M. H., & Ekers, R. D. 2000a, A&AS, 146, 31
Prandoni, I., Gregorini, L., Parma, P., de Ruiter, H. R., Vettolani, G., Wieringa, M. H., & Ekers, R. D.2000b, A&AS, 146, 41
Prandoni, I., Gregorini, L., Parma, P., de Ruiter, H. R., Vettolani, G., Zanichelli, A., Wieringa, M. H., & Ekers, R. D. 2001, A&A, 369, 787
Rawlings, S., Eales, S., & Lacy, M. 2001, MNRAS, 322, 523
Rengelink, R. B., Tang, Y., de Bruyn, A. G., Miley, G. K., Bremer, M. N., Röttgering, H. J. A., & Bremer, M. A. R. 1997, A&AS, 124, 259
Richards, E. A. 2000, ApJ, 533, 611
Richards, E. A., Fomalont, E. B., Kellermann, K. I., Windhorst, R. A., Partridge, R. B., Cowie, L. L., & Barger, A. J. 1999, ApJ, 526, L73
Sault, R. J., & Conway, J. E. 1999, in ASP Conf. Ser. 180, Synthesis Imaging in Radio Astronomy II, ed. G. B. Taylor, C. L. Carilli, & R. A. Perley (San Francisco: ASP), 419
Sault, R. J., Teuben, P. J., & Wright, M. C. H. 1995, in ASP Conf. Ser. 77, Astronomical Data Analysis Software and Systems IV, ed. R. A. Shaw, H. E. Payne, & J. J. E. Hayes (San Francisco: ASP), 433
Wall, J. V. 1994, Australian J. Phys., 47, 625
White, R. L., & Becker, R. H. 1992, ApJS, 79, 331
Windhorst, R. A., Hopkins, A., Richards, E. A., & Waddington, I. 1999, in ASP Conf. Ser. 193, The Hy Redshift Universe, ed. A. J. Bunker & W. J. M. van Breugel (San Francisco: ASP), 55